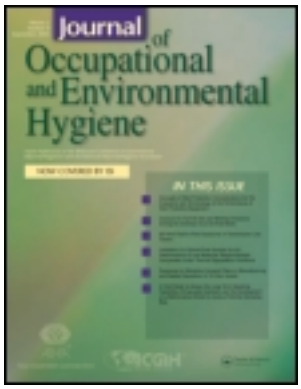

Journal of Occupational and Environmental Hygiene
Publication details, including instructions for authors and subscription information:
http://www.tandfonline.com/loi/uoeh20

Headform and N95 Filtering Facepiece Respirator Interaction: Contact Pressure Simulation and Validation

Zhipeng Lei [a] , Jingzhou (James) Yang [a] & Ziqing Zhuang [b]

[a] Human-Centric Design Research Lab, Department of Mechanical Engineering, Texas Tech University, Lubbock, Texas

[b] National Institute for Occupational Safety and Health, Pittsburgh, Pennsylvania

Available online: 14 Dec 2011

To cite this article: Zhipeng Lei, Jingzhou (James) Yang & Ziqing Zhuang (2012): Headform and N95 Filtering Facepiece Respirator Interaction: Contact Pressure Simulation and Validation, Journal of Occupational and Environmental Hygiene, 9:1, 46-58

To link to this article: http://dx.doi.org/10.1080/15459624.2011.635130

Journal of Occupational and Environmental Hygiene, 9: 46–58
ISSN: 1545-9624 print / 1545-9632 online

DOI: 10.1080/15459624.2011.635130

Headform and N95 Filtering Facepiece Respirator Interaction: Contact Pressure Simulation and Validation

Zhipeng Lei,[1] Jingzhou (James) Yang,[1] and Ziqing Zhuang[2]

[1]Human-Centric Design Research Lab, Department of Mechanical Engineering, Texas Tech University, Lubbock, Texas,
[2]National Institute for Occupational Safety and Health, Pittsburgh, Pennsylvania

This article presents a computational and experimental study of contact pressure between six N95 filtering facepiece respirators (FFRs) and five newly developed digital headforms (small, medium, large, long/narrow, and short/wide). Contact interaction is simulated using the finite element method and validated by experiments using a pressure mapping system. The headform model has multiple layers: a skin layer, muscle layer, fatty tissue layer, and bone layer. Each headform is divided into five parts (two parts for the cheeks, one part for the upper forehead, one part for the chin, and one part for the back side of the head). Each respirator model comprises multiple layers and two straps. The simulation process has two stages for each respirator/headform combination. The first stage is to wrap the straps around the back of the headform and pull the respirator away from the face. The second stage is to release the respirator so that the respirator moves toward the face. Strap forces and contact interactions are generated between the respirators and the headforms. Meanwhile, a real-time surface pressure mapping system is used to record the pressures at six key locations to validate the computational results. There is a strong correlation between computational and experimental results ($R^2 = 0.88$). By comparing the pressure values from simulations and experiments, we have validated the simulation models.

Keywords digital headform, FE method, fit and comfort, respirator, stress and strain

Correspondence to: James Yang, Human-Centric Design Research Lab, Department of Mechanical Engineering, Texas Tech University, Lubbock, TX 79409; e-mail: james.yang@ttu.edu.

The findings and conclusions in this paper are those of the authors and do not necessarily represent the views of the National Institute for Occupational Safety and Health.

INTRODUCTION

Filtering facepiece respirators (FFRs) are commonly used for personal protection from exposures to respirable aerosol particles. Respirator comfort and fit are two important parameters for respirator designers, manufacturers, users, and standards developers. Many factors affect respirator comfort and fit, such as user anthropometry, respirator material, strap forces, and so on. This article attempts to develop and validate a computational method for the contact pressure between a headform and a N95 FFR. The ultimate goal is to develop predictive models to virtually assess respirator comfort and fit to reduce the cost of design and shorten the time to market.

Significant research has been done in terms of the experimental approaches for respirator comfort and fit.[1–14] However, these experimental approaches are time-consuming and expensive. For example, Cohen[9] used both a fit validation system and a pressure measurement system. These two systems cost about $6000 each and require 90 min per subject to test respirator fit and contact pressure distribution (comfort).

A few researchers have developed respirator and headform models and simulated respirator/headform interactions. Bitterman[15] used the finite element (FE) method to calculate the pressure between an oxygen mask and pilot's face. The model of the pilot's face was simplified as a rigid surface without any deformation. Piccione et al.[11] applied a FE analysis tool, DYNA3d, which is an explicit 3D code and an older version of LS-DYNA (preprocessing software), to create deformable human face and respirator models. Zhuang and Viscusi[16] developed five standard digital headform models representative of U.S. civilian respirator users by using principal component analysis. Yang et al.[17] used the medium-sized headform model[16] and 3D scan of one respirator model to build FE models as shell elements. The FE models were then used for a sensitivity analysis of important parameters affecting contact pressure.[18] The relationship of pressure distribution and respirator fit and comfort was also discussed by Dai et al.[18] All of these simulations adopted a simplified headform that has single layer structure and could not precisely represent an anatomically correct human head. Zhuang et al.[19] updated the five standard headforms, and Lei et al.[20] used the updated headform models to build high fidelity FE models for contact simulation.

Deformable modeling of the human head has been widely used in many applications, such as animation of facial expression and surgical simulations. In the field of realistic animation, a deformable mass-spring tissue model that creates facial animation by a layered mass spring tissue was introduced.[21] The mass-spring layer is a simplified elastic model, so the computation is efficient but is unable to provide realistic results of facial soft tissue.[22] Meanwhile, an FE tissue model that approximates the continuum of facial tissue by deconstructing it into elements was developed.[23] Couteau et al.[24] obtained patient data (CT scans and MRI) and generated an FE model of the patient face by a "mesh-matching" algorithm. Payan et al.[25] modeled different tissue layers and explicit representation of face muscles by distinct constitutive equations. Luboz et al.[26] introduced a mesh generating algorithm that can automatically mesh a patient's face for facial tissue modeling. Zhang et al.[27] described a better method to build a multilayered face model from the scanned surface data. Barbarino et al.[28] proposed a 3D FE model of the face and validated it through measuring the facial tissue response to gravity loads. None of the above studies validated contact pressure between a respirator and headform.

The objective of this study was to simulate and validate the contact pressure between the human face and an FFR using high biofidelity headform and respirator models based on previous work[20] and the five new headforms.[19] The contact pressure distribution is obtained through simulation, and the computational results are validated by experiments.

First, this article introduces FE models for both headforms and FFRs. Headform models are originated from 3D scanning surfaces of subjects (large, long/narrow, medium, short/wide, and small). Based on head anatomy, a high biofidelity headform model is separated into frontal, maxilla, mandible, and back head parts. Each part has multiple layers, including skin, muscle, fat tissue, and bone. Note that the deformable multilayer headforms are critical to account for the effect of deformability on the contact pressure in this study. Three sizing systems of FFRs, including one-size respirator, two-size respirator (small and medium/large), and three-size respirator (small, medium/large and X large), are also created with multilayer structures and strap components.

Second, the simulation process is analyzed and designed as two stages. The first stage is to wrap the straps around the back of the headform and pull the respirator away from the face. The second stage is to release the respirator so that it moves toward the face. Different strap forces and contact interactions are automatically generated between the respirators and the headforms. Third, experiments are described. Contact pressures on the interface between the respirators and headforms are measured to validate the simulation results. A real-time surface pressure mapping system is used to record the pressures at six key locations of human faces. Fourth, detailed experimental results that validate the simulations are presented. Finally, discussions and conclusions are given.

METHODS AND MATERIALS

Anatomy of the Human Head

To build accurate deformable headform models the anatomy of the human head has to be studied and well understood. Epidermis and dermis are the two major layers of facial skin.[22,29] The outer layer is the epidermis, a superficial 0.06 mm–0.1 mm thick layer of dead cells. The underlying dermis layer is 0.5–3.5 mm thick and is responsible for the elasticity of the skin. Subcutaneous fatty tissue presents beneath the skin and its thickness varies over the human face. Many facial muscles exist between the facial skin and the underlying bone structure. The soft tissues including the skin, fatty tissue, and muscle contribute to the elastic behaviors. When the head is fixed, the facial bones are considered as the boundaries that constrain the deformation of the soft tissues.

In the case of respirator contact, the interactions primarily happen on the frontal, maxilla, and mandible regions where the frontal region includes the nasal bridge. Thus, these three areas should be modeled as deformable parts, and other areas of the head can be simplified as rigid bodies.

Structure of FFRs

Although different types of FFRs are available on the market, they have similar structures. The structure has several layers, typically including a soft inner seal, comfortable inner lining, and filtration layers. A flexible nosepiece and elastic head straps are also featured in most FFRs. The contact behavior is mainly a function of the seal area and the straps, while other components of the respirator can be neglected.

General Procedure of FE Simulation

The procedure for developing FE models includes several stages as shown in Figure 1. First, the original models in the form of point clouds are obtained by scanning respirator samples or human subjects. Second, computer-aided design (CAD) models are generated from digital headforms or the scanned respirator data through two middle stages from the point cloud: polygon and non-uniform rational B-spline (NURBS). The CAD models' quality is improved by removing deficiencies in shape. Third, shell and solid elements are generated by

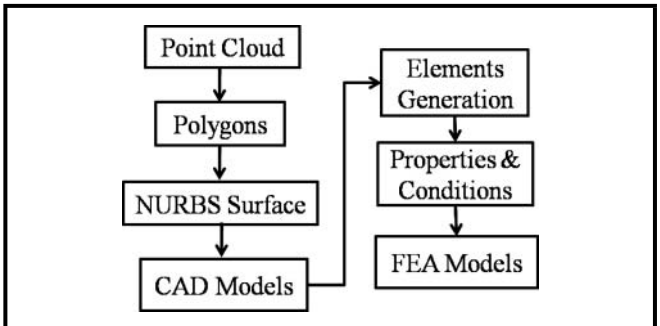

FIGURE 1. Flow chart of modeling procedure.

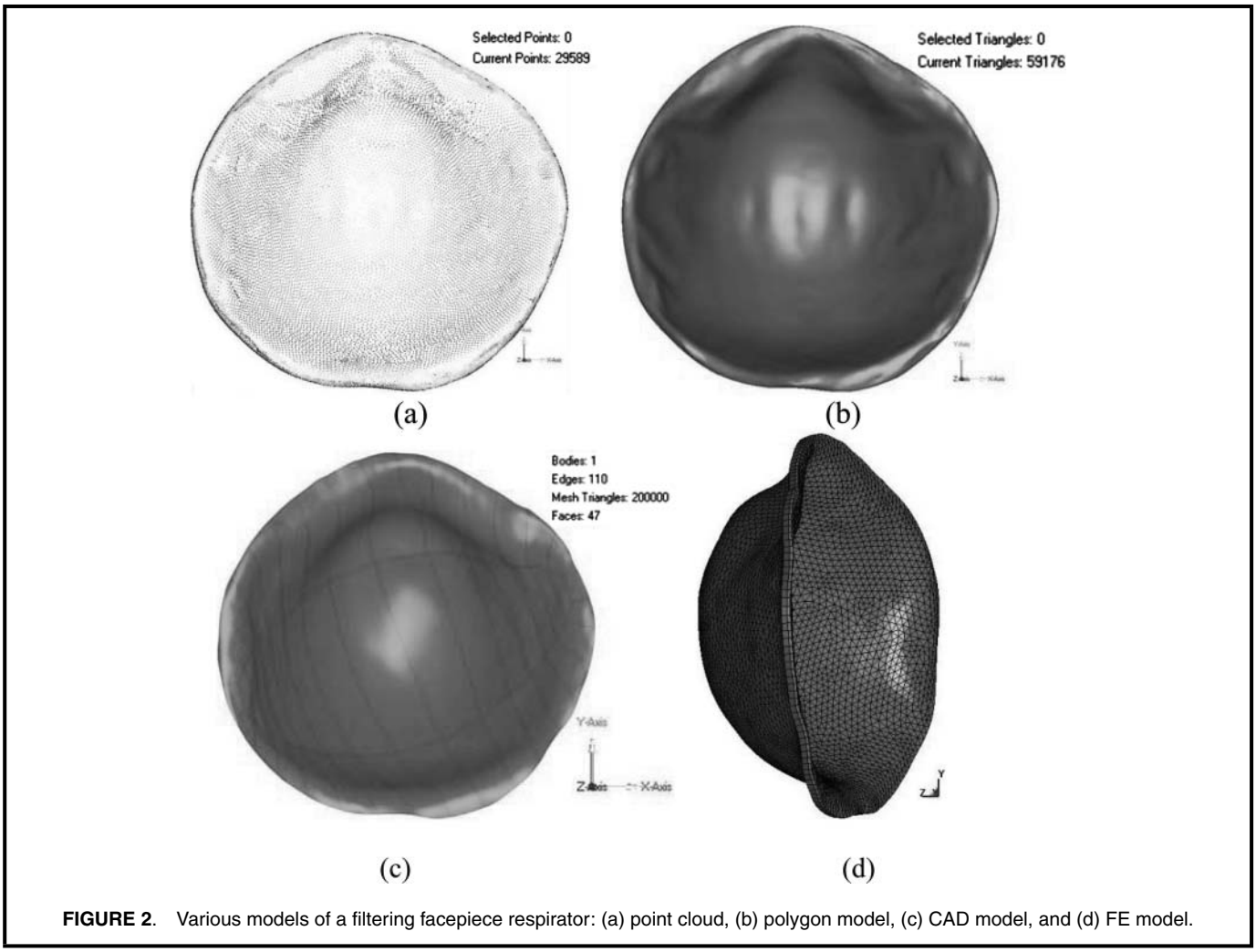

FIGURE 2. Various models of a filtering facepiece respirator: (a) point cloud, (b) polygon model, (c) CAD model, and (d) FE model.

meshing the CAD models. Finally, material properties, and boundary and initial conditions are applied to prepare the FE models for analysis.

3D scanning is the most feasible and accurate way of capturing surfaces of complex shapes such as FFRs and headforms. A 3D scanner emits laser radiation and detects its reflection for evaluating the surface of an object. The data obtained from the 3D scanner are point clouds. These raw data cannot be directly manipulated in FE analysis.

Polygon and NURBS models are two middle stages between point clouds and CAD models. The polygon model is made up of a large number of triangles that are generated by connecting adjacent three points in the point cloud. Then, a NURBS surface model is created by fitting a reproducible surface to the underlying polygons. The CAD model can be obtained by transforming the NURBS model. Holes, spikes, and noise may be generated during scanning due to the complexity of respirator and headform shapes. If the deficiencies in the CAD model cannot be overcome, a few iterations may be required to improve the models. Note that although the polygon models can be sent directly to the FE preprocessor, the element quality of the polygon models is usually not enough for FE analysis. Available FE preprocessing software is not good enough for remeshing highly curved surface from polygon models. Thus, transferring the polygon models into the CAD models is necessary.

FE Models of FFR

An FFR with only one size is used as an example to demonstrate how to build FE models of FFRs. Figure 2a shows a point cloud model of the FFR, which is generated by scanning the shape of the respirator. Figure 2b gives its polygon model in which holes are filled, spikes and noise are removed, and the surface is relaxed. This polygon model is a manifold closed surface, including both inner and outer faces. Since a multilayer FE model will be generated, only the inner face is kept for further usage and the outer face is removed. Figure 2c presents the CAD model of the respirator as a single shell that comes from the inner surface of the respirator. This shell consists of 47 curved faces, perfectly manifesting the shape of the respirator.

Through the study of respirator structure, the FE model of the respirator is designed to have an inner face sealing layer and outer layer. After importing the CAD model into LS-DYNA preprocessing software, the shell surface is divided into as

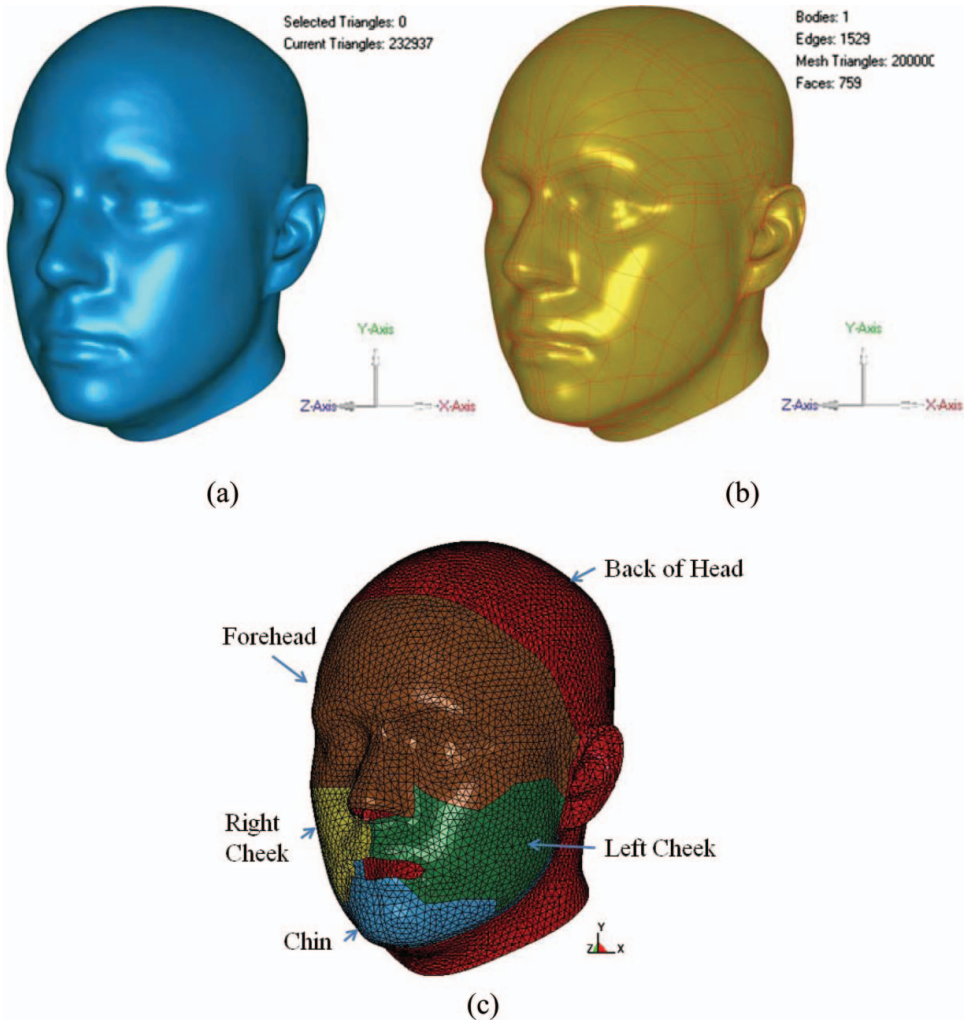

FIGURE 3. Headform models: (a) polygon model, (b) CAD model, (c) FE model.

triangle elements. Then this shell surface is offset and two layers of pentahedron solid element are obtained, representing two different materials. As shown in Figure 2d, the inner layer of the respirator has a 1 mm thickness, and the outer layer has a 2 mm thickness. Models of the two straps are built independently using the length and width that are measured from the respirator sample.

FE Models of Headforms

Figure 3a shows the polygon model of the medium-sized headform with 232,937 triangles. To transform it to a CAD model, parts of complex shape require special treatment. The ear area is the most intricate part of the headform. Because the polygon model of the headform has low quality in the ear area, spikes and holes are carefully removed by hand, and the shape is relaxed to the extent that does not diminish its main shape features. Eyes, nose, and mouth parts are also complex and are treated in an identical manner. Figure 3b shows the CAD model of the headform with 759 curved faces.

As discussed in anatomy of human head section, the human headform can be divided into five parts, with different thickness and components. By using the LS-DYNA preprocessing function, one can trim and divide the CAD model of headform into five parts. Figure 3c shows the divided headform model, including forehead, left cheek, right cheek, chin, and back of the head. The surfaces of these five parts can be meshed into triangular shell elements.

The back of the head is treated as a rigid shell to reduce computational time. Facial parts have multilayer structures, in which the skin layer is at the top level of the headform surface, and the bone layer is at the bottom level of the headform. First, the forehead, cheek, and chin are offset separately, generating skin layers. Then, the inner surface of the skin layer is extracted and offset toward the headform core to generate a muscle layer. The fatty tissue and bone layers are created in the same way. Through this procedure, we can easily define the structure of each facial part and give a different thickness to each layer.

At different locations over the human face, the facial soft tissue varies in its structure and layer thickness. References

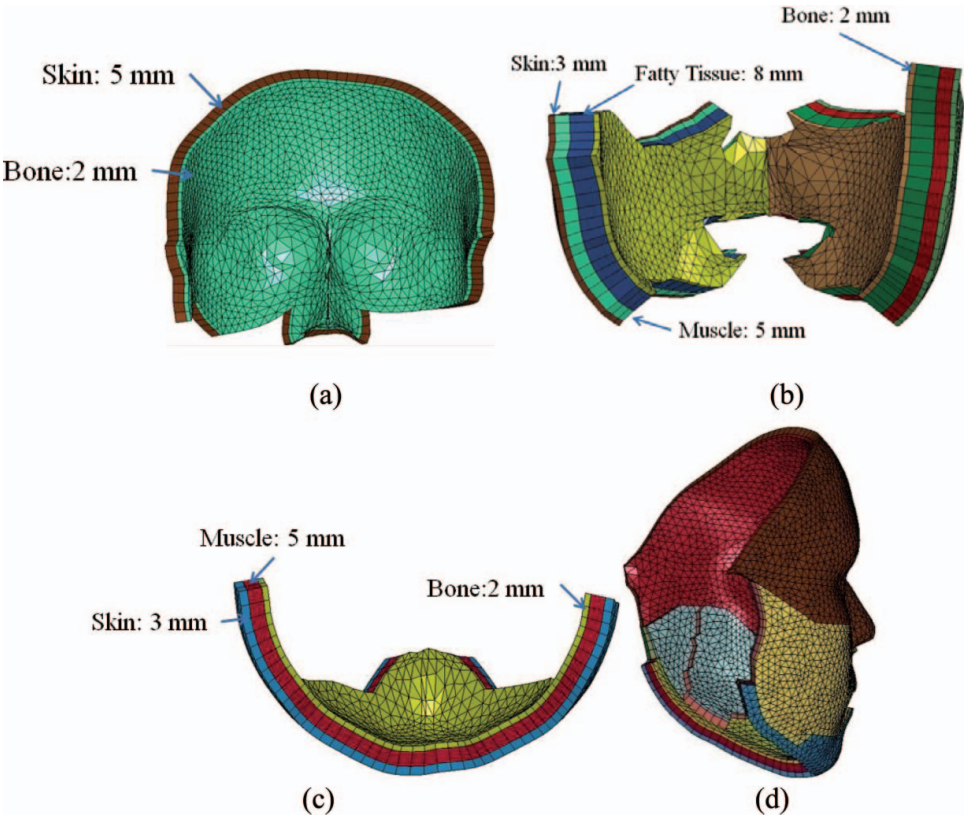

FIGURE 4. Layers for the headform: (a) forehead part, (b) left and right cheek parts, (c) chin part, (d) four front face parts together.

from Takema et al.[30] and De Greef et al.[31] are used as input. In Figure 4, the forehead has 5 mm thick skin and 2 mm thick bone; the left and right cheek have 3 mm thick skin, 5 mm thick muscle, 8 mm thick fatty tissue, and 2 mm thick bone; the chin has 3 mm skin, 5 mm thick muscle, and 2 mm thick bone. Finally, the headform FE model is made up of 13,570 pentahedron solid elements for FE analysis.

Mechanical Properties

We assign the layers of the respirator as elastic materials. The inner face seal layer has mechanical properties of density of 1.39 g/m^3, Young's modulus of 27.7 MPa, and Poisson's ratio of 0.37. Note that Young's modulus is a measure of the stiffness of an elastic material and is a quantity used to characterize materials. Poisson ratio is the ratio of the fraction (or percentage) of expansion divided by the fraction (or percentage) of compression, for small values of these changes. The outer comfortable layer has mechanical properties of density of 1.39 g/m^3, Young's modulus of 7 M Pa, and Poisson's ratio of 0.40.[32] We have conducted several tensile tests in the material lab at Texas Tech University for measuring the mechanical properties of respirator straps. From these experiments, a Young's modulus of 10.2 MPa and Poisson's ratio of 0.3 to the straps of the one-size FFR were obtained.

For the FE models of headforms, accurate material properties of each layer are critical to having correct simulation results. Although there is a large body of literature on mechanical properties of human tissue, there is no reported exact, comprehensive, and representative data of the human face. Factors such as sex, age, size, and so on, increase the scatter and uncertainty in the material properties of human tissue.[33] The elastic material properties of layers for headform models used in the work are adapted from Fung[34] and Duck[35] shown in Table I. The bone and the back of the head are defined as rigid bodies.

Strap Deformation

The simulation process is used to study the interactions between FFRs and human headforms in a computational

TABLE I. Mechanical Properties of Headform Layers

Layer	Density (g/m^3)	Young's Modulus (M Pa)	Poisson's Ratio
Skin	1.20	0.6	0.45
Muscle	1.06	0.79	0.42
Fatty tissue	1.00	0.015	0.48
Bone (rigid)	4.50	1000	0.30
Back of head (rigid)	4.50	1000	0.30

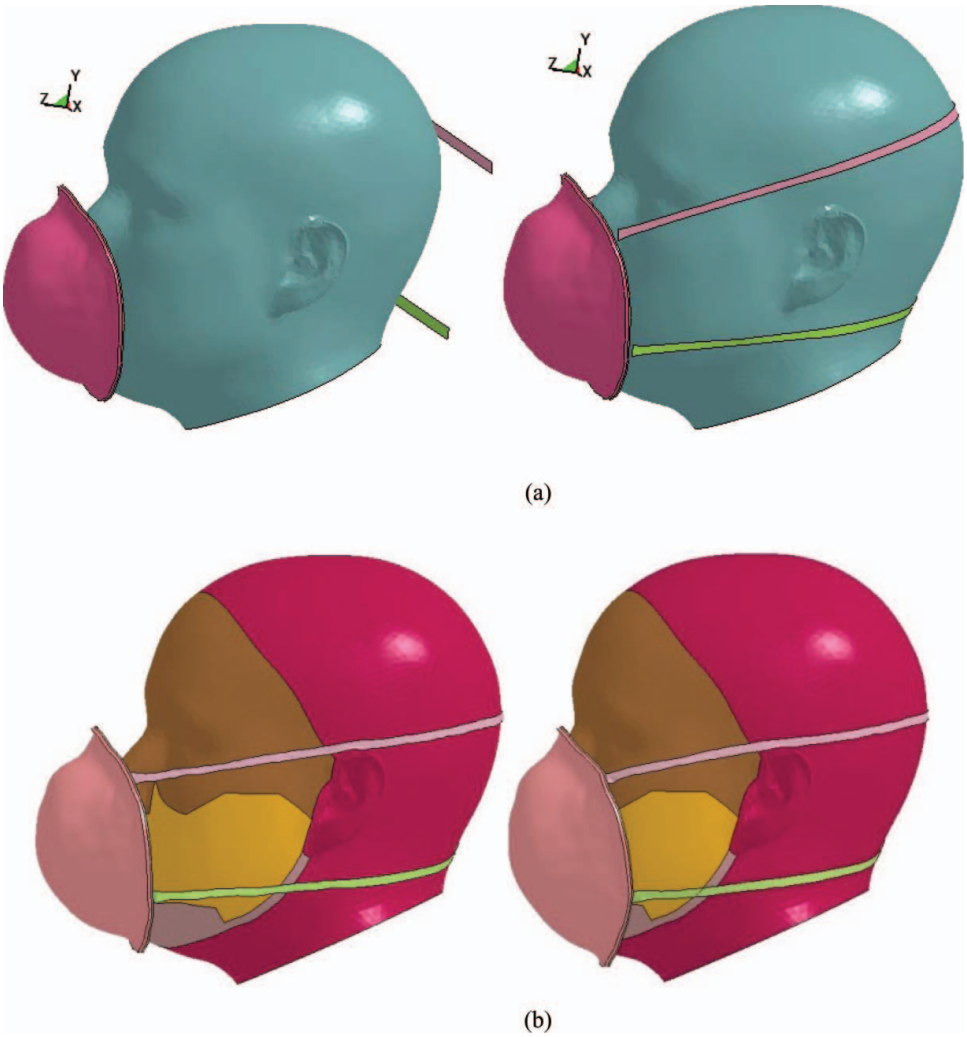

FIGURE 5. Simulation procedure: (a) Stage I, the initial and the ending states; (b) Stage II, the initial and the ending states.

environment. When a user wears an FFR, the top strap is pulled over the head and rests high at the top of the back of the head (occiput), while the bottom strap is pulled over the head and is positioned around the neck below the ears. Thus, contact happens not only between the respirator and the human face but also between the respirator straps and the human head. The magnitudes and directions of strap forces are automatically determined by the deformation of the straps. In previous FE simulations of respirator or mask contact reported in the literature, straps were not included in the model.[9,11,15,17,20] In these simulations, the researchers had difficulty determining the shape and deformation of straps, since they are related to the size and shape of the headform and the lengths and mechanical properties of the straps. In these simulations, the magnitude and orientation of strap forces were predefined. However, in the real world, different headforms and respirator combinations have different strap force magnitude and orientations. It is difficult to apply these precisely in this simulation environment. Therefore, in this article we have incorporated strap models into the simulation to automatically generate the strap forces (magnitude and orientation) according to the respirator and headform geometries.

To incorporate straps into the simulation, material properties were obtained by directly measuring FFR samples. The simulation procedure includes two stages: strap deformation (Stage I) and respirator contact (Stage II).

Stage I wraps the straps along the back of the headform, as shown in Figure 5a. The FE models of the respirator, headform, and straps are placed in the same global coordinate system, in which the z coordinate is in the normal direction to the headform frontal face, the x coordinate is along the lateral direction of the headform, and the y coordinate is along the vertical direction of the headform.

The two straps of the respirator have the same lengths and mechanical properties. At the initial state, the respirator is positioned in front of the headform and about a 3-mm gap is maintained between the respirator and headform. The alignment of the respirator with the headform is critical for the simulation. In the real world, respirator users first put on the respirator, then readjust the respirator to ensure the most

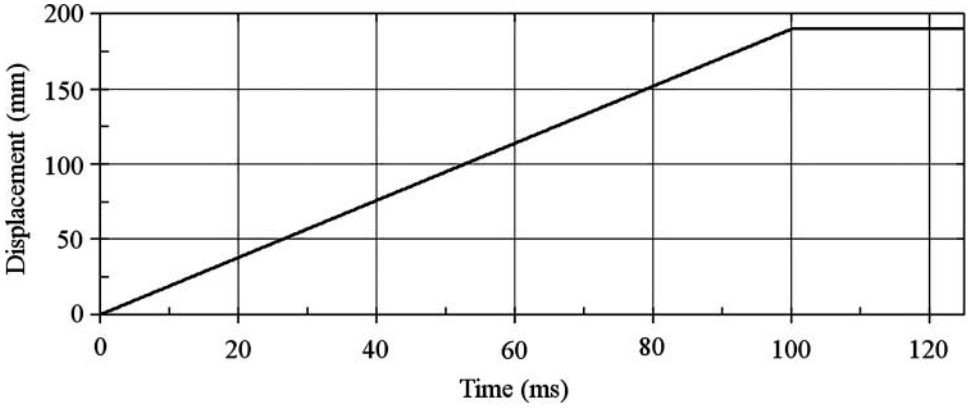

FIGURE 6. The displacement vs. time curve of one strap end in z direction.

comfortable position. But in this research work, we use the following procedure to align the respirator with the headform: (1) define a vertical plane on the respirator model that is perpendicular to the plane of symmetry, (2) ensure this vertical plane of the respirator is parallel to the coronal plane of the headform, and (3) align the respirator symmetric plane with the sagittal plane to be overlapped. The top strap is located at the top of the back of the headform, and the bottom strap is around the neck below the ears. With the respirator in a stationary position, the two ends of each strap are pulled toward the respirator until the straps reach the respirator. As this occurs, the straps are wrapped along the back of the headform.

Simulation of this stage includes four FE models: the headform, the respirator, and two straps. The headform and respirator models are made of pentahedron solid elements. Each pentahedron solid element has six nodal points. Boundary conditions for Stage I are defined as follows: the displacements of all six degrees of freedom for both the headform and respirator are zero. Two strap models are made of rectangular shell elements with deformability. Each shell element has four nodal points. The pressure and stresses of each point are determined by its displacement ($u(t)$). So, the mathematical objective of the FE analysis is to calculate $u(t)$ of each nodal point on the straps. Since our FE models use linear and elastic material, the $u(t)$ value of any arbitrary nodal point can be obtained by solving the equation of motion for linear elasticity

$$m\ddot{u}(t) + c\dot{u}(t) + ku(t) = p(t), \qquad \textbf{(1)}$$

where m is the mass of the element to which the nodal point belongs, c is the damping coefficient, and k is the stiffness of the element. The terms $m\ddot{u}$, $c\dot{u}$, ku and $p(t)$ indicate the inertial force, viscous damping, linear elasticity, and time-dependent loading, respectively. The values of m,c, k and $p(t)$ are given, while u is unknown and is calculated by LS-DYNA's solver. Once the displacement (u) of each node is determined by solving Eq. 1, the deformation and internal stress of each shell element on straps can be obtained. This provides the input for Stage II.

The displacement of the nodes at the strap ends, which are different for each pair of headforms and respirators and are related to the lengths of straps and size of the headform, are defined and constrained. A boundary condition of prescribed displacement is imposed globally by setting the constrained acceleration components to zero. For nodes on the ends of straps, the displacement versus time curves in x, y, and z directions are defined. Then, the displacement vs. time curve is differentiated to generate the velocity vs. time curve. Figure 6 shows that nodes on straps have a constant velocity during the time period 0–100 ms and stay fixed during the time 100–200 ms.

During the time period of 0–100 ms, the nodes on the strap ends have very high velocities, which give other nodes of straps high time-dependent loading ($p(t)$). According to Eq. 1, out of range acceleration and velocity, caused by a high $p(t)$, can make the system unstable unless a large enough damping coefficient (c) is given. A global damping coefficient ($c = 0.5m \sim 3m$) is applied for maintaining acceleration and velocity at a low level. During the time period of 100–200 ms, due to the damping force, the whole system becomes quiescent. Meanwhile, a contact is defined between the straps and the headform with LS-DYNA's explicit contact solver. The contact and boundary conditions work together to deform the straps and to generate their internal stresses. In the final state of Stage I, LS-DYNA software automatically exports coordinates and stresses of all nodes as the input of Stage II.

Respirator and Headform Interaction

Stage II releases the respirator and allows the respirator to contact the headform. We also constrain the displacements of nodes on the back of the head and the bone layers of the forehead, right cheek, left cheek, and chin segments. While the model of the two straps and the model of the respirator are separated in Stage I, they are combined in Stage II. Shell elements are created for linking the respirator and strap ends, as shown in Figure 7.

Consider the deformed straps that are extracted from Stage I as shown in Figure 5b. At the initial state, the respirator model

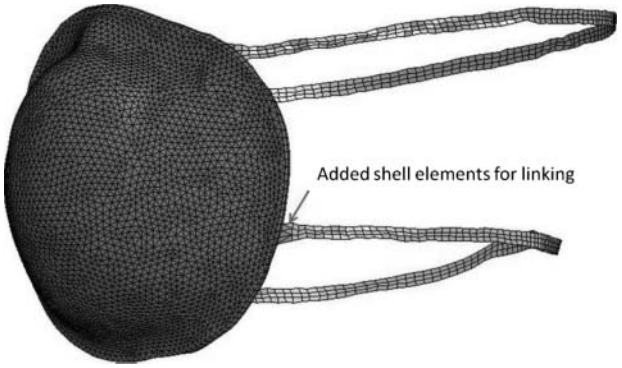

FIGURE 7. Shell element for linking the respirator and the straps.

is in the same position as in Stage I. Potential energy stored in the straps contributes to the movement of the respirator towards the headform. Two contacts exist: the first contact is between the respirator and the headform, and the other one is between the straps and the headform. At the ending state, the respirator rests on the headform. Although the potential energy of the straps now is much less than that at the initial state, it still provides forces on the respirator to generate contact pressure. We conduct the simulation of Stage II to obtain contact pressure distribution between the respirator and the headform.

The internal stresses of the two straps drive the respirator to contact the headform and the straps also contact the headform. Thus, a 3D algorithm for surface-surface contacts is defined in LS-DYNA preprocessing. The headform surface is modeled as the master segment, while the surfaces of the respirator and straps are modeled as the slave segment.

The penalty method is used in the contact algorithm. In Figure 8, s denotes the master surface (segment) and **n** is the slave node. The contact point **c** is the nearest point to the slave node **n** on the master surface s. The slave node **n** is located in element i and the master surface s has element j. In each

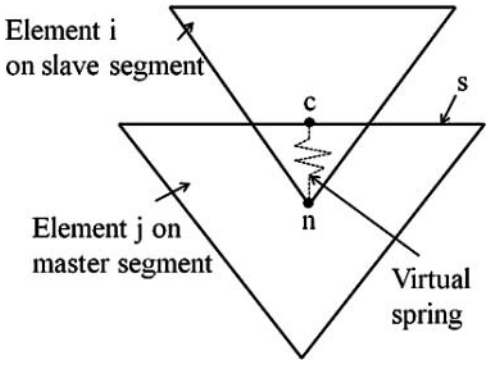

FIGURE 8. The virtual spring placed between the contact point **c** and the slave node **n**.

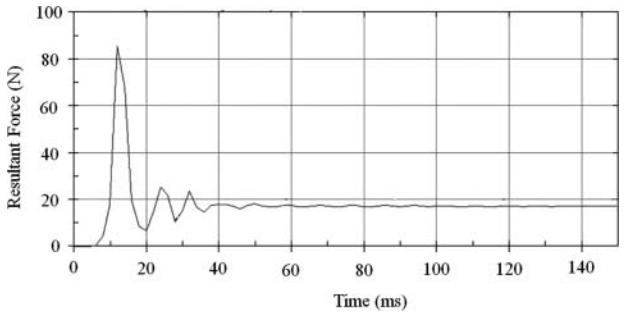

FIGURE 9. Resultant force profile of headform.

time step, the penetration between the slave node **n** and the master surface s is checked. When the slave node penetrates the master surface, a virtual spring is added between the contact point **c** and the slave node **n**. The direction of the spring force is parallel to the normal direction of the master surface, and the magnitude is proportional to the depth of penetration. As a consequence, the spring force changes the shapes and motions of both elements, and the penetration between them is eliminated. Because the stiffness of the headform skin layer is relatively small compared with the stiffness of the respirator, the contact simulation can easily break down. A formula, determining the stiffness k of a contact spring, is elaborately selected as follows:

$$k = 0.1\frac{m}{\Delta t^2}, \quad \textbf{(2)}$$

where m is the mass of element j on the master segment and Δt is the global time step size.[36]

In Stage II, every contacting element of the slave segment is given a viscous contact damping force. The damping force, $2mwv$, where m,w, and v are the mass, natural frequency and velocity of the element, is applied in the negative normal direction of the master surface that has the contact point.

LS-DYNA's explicit solver calculates the motion of models during the time period of 0–150 ms. Figure 9 shows the resultant force of the headform surface versus time. The highest value appears at the time of 11.99 ms and keeps constant after 133.99 ms. When the resultant force of the headform surface becomes constant, the whole system becomes stable and results may be output.

Experimental Materials

Six FFRs from three different sizing systems are used: one from the one-size respirators, two from the two-size respirators (medium and small), and three from the three-size respirators (X-large, large/medium, and small). Prototypes of five size headforms are produced by American Precision Prototyping, LLC with Polypro-Like Accura 25 material. The surfaces of the prototypes are non-deformable and detailed facial features, and sizes are identical to the National Institute for Occupational Safety and Health (NIOSH) models.[19] Note that we used the non-deformable headform prototypes for validation because deformable headform prototypes are too expensive.

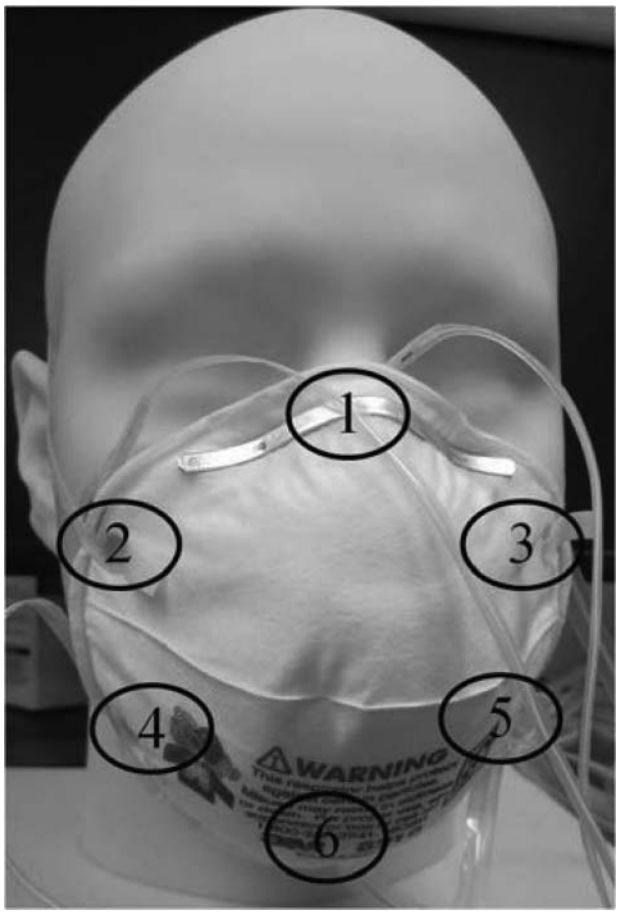

FIGURE 10. Six sensors are located on the key areas: (1) nasal bridge, (2) top of right cheek, (3) top of left cheek, (4) bottom of right cheek, (5) bottom of left cheek, and (6) chin.

The Tactilus freeform sensor system (Sensor Products Inc., Madison, N.J.) is used for the experiments. Sixteen separate sensor elements with thin and tactile surface are available for conducting measurements on surfaces with complex geometries such as a human face. Each sensor element is in the shape of 1 cm^2 square and has $1mm$ thickness. The user can place sensors at desired locations. The hub collects the pressure data and sends the data to the computer by a cable. Tactilus software collects and stores the results.

The Tactilus freeform sensor system was calibrated before measurements of contact pressure. The calibration comprises three steps. First, lay the sensor elements on a plate desk and remove any external sources of forces acting on the surfaces of the sensor elements. Second, carefully place weights (Sto-A-Weigh weight set; Ohaus Scale Corp., Florham Park, N.J.) on the top surfaces of the sensor elements, while recording the pressure data measured by the sensor system. In this step, a 20-g weight is always placed directly on the sensor element, acting as a base, because its shape can cover the top face of the sensor element and hold other weights. Fifty-gram, 100-g, and 200-g weights are put up on the 20-g weight separately. Pressures on each sensor element, generated by the weight combinations

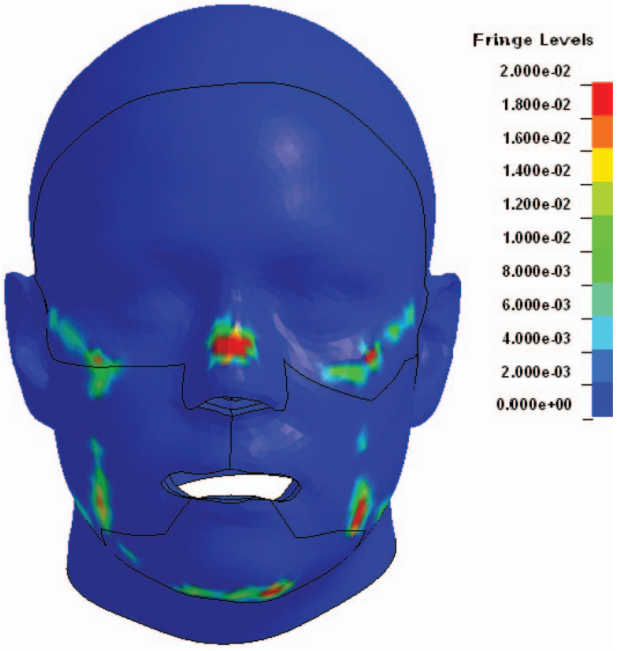

FIGURE 11. Pressure distribution from the simulation.

that include 20-g, 70-g, 120-g, and 220-g total weights, are measured and recorded. Third, analyze the data for accuracy. We assumed that the sensor element surface fully contacts the weight with a contact area of 1 cm^2 and the pressure can be calculated (as total weight/contact area). Measured pressures are compared with calculated pressures. We found that the accuracy of the sensor system is $\pm 3\%$.

Experimental Procedures

It is not practical to measure the pressure of all contact points. Therefore, in this study, key areas are selected and pressure sensors are deployed in these areas (Figure 10). Since we have six FFRs (one-size respirator, small and medium FFRs of two-size respirators, X-large, large/medium, and small FFRs of the three-size respirators) and five headforms (large, medium, small, short/wide, and long/narrow), there are 30 combinations of respirator and headform combinations. For the purpose of comparison, the contact pressures on the six key areas are obtained from both the experiments and the simulations. These six key areas are selected for validation shown in Figure 11. All experiments were repeated three times, generating (3×180) 540 records of contact pressures, while the simulations produce 180 pressure records.

A tiny change in sensor location could change the pressure value dramatically. The experimental pressure at a certain point should be compared with the computational pressure at the same point. However, it is difficult to ensure the exact same location for experimental and computational cases.

For each test, there are several steps. First, put the FFR on the headform and make sure the respirator straps are in the correct position. Second, insert six sensors between the FFR and the headform. Third, carefully adjust the position of the

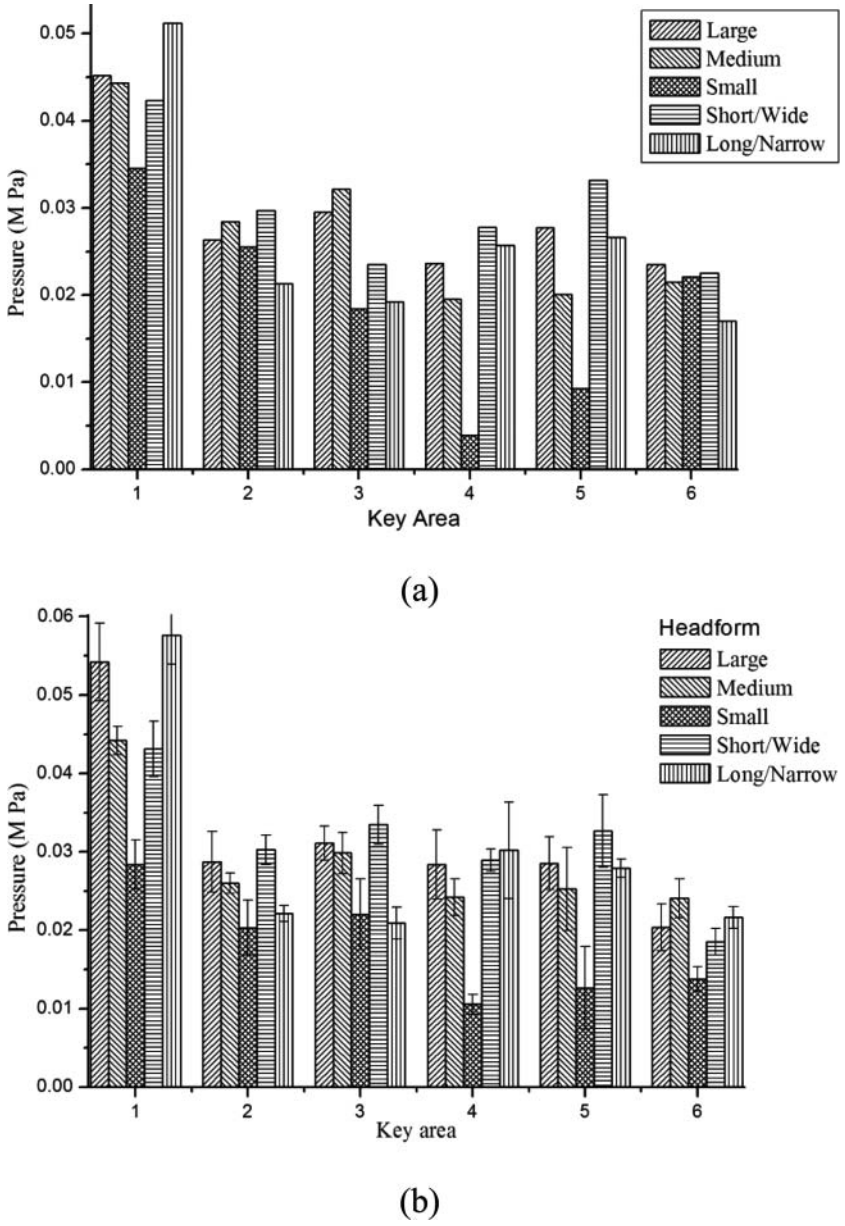

FIGURE 12. Contact pressure values for the filtering facepiece respirator of the one-size only system on five headforms: (a) computational results, (b) experimental results.

sensors until the highest pressure value is obtained. Finally, read and record pressure values.

RESULTS

Figure 11 shows the pressure distribution from the contact simulation. The results from experiments and simulations show that six locations exhibit the highest pressures: the nasal bridge, top of left cheek, bottom of left cheek, top of right cheek, bottom of right cheek, and chin. For other respirator and headform combinations, the results are similar.

Figure 12 depicts the contact pressure values for the one-size respirator with five headforms on six key areas. Figure 12a gives the computational results and Figure 12b presents the average values and their standard deviations (SD) resulting from experiments. Similarly, one can obtain the contact pressure values for two-size and three-size respirators.

Tables II to IV summarize the contact pressure differences between experiment and simulation and the SD of the three repeated experiments. Among the 180 pairs of pressure records, the pressure differences are all below 0.0100 MPa and 142 of them are within ± 0.0050 MPa. This result shows that pressure difference is very small. We also provide linear regression analysis for computational and experimental results. As shown

TABLE II. Contact Pressure Differences and SD (M Pa) for the Respirator of One-Size Only System

	One-Size Respirator					
	Key Area					
Headform	**1 (SD)**	**2 (SD)**	**3 (SD)**	**4 (SD)**	**5 (SD)**	**6 (SD)**
Large	–0.0090 (0.0050)	–0.0024 (0.0039)	–0.0016 (0.0022)	–0.0048 (0.0044)	–0.0008 (0.0034)	0.0031 (0.0030)
Medium	0.0001 (0.0018)	0.0024 (0.0013)	0.0022 (0.0026)	–0.0047 (0.0023)	–0.0052 (0.0053)	–0.0026 (0.0025)
Small	0.0061 (0.0032)	0.0052 (0.0035)	–0.0036 (0.0045)	–0.0067 (0.0013)	–0.0034 (0.0053)	0.0083 (0.0015)
Short/wide	–0.0008 (0.0035)	–0.0006 (0.0019)	–0.0100 (0.0025)	–0.0011 (0.0014)	0.0006 (0.0046)	0.0040 (0.0017)
Long/narrow	–0.0064 (0.0037)	–0.0009 (0.0010)	–0.0017 (0.0020)	–0.0045 (0.0062)	–0.0013 (0.0011)	–0.0046 (0.0014)

in Figure 13, the horizontal axis is the simulation value, and the vertical axis is the experimental value. The R^2 value is 0.8803, indicating a strong correlation, and the P value is 0.0013, indicating a high confidence.

In post-processing, the computational results of the shear distributions, the facial deformations, and the strap forces can be obtained. Through a literature review, it was determined that only a few experimental approaches are available for comparing these results. The shear distributions and the facial deformations are related to the skin comfort. The strap forces can be used in the respirator design.

DISCUSSION

Because the headform FE models were generated from 3D scanned data of human subjects, the geometry features of the human head can be well maintained. However, significant effort was required to resolve the deficiencies of the scanned complex geometry of the headform. The structures of multiple layers and the definitions of soft tissue properties gave the headform models the capability of deformation. It was found that accurate material properties are critical to the simulation-based approach. Furthermore, careful treatment of penetration conditions and parameters in LS-DYNA implementation is needed.

The six areas of the headform, which have the highest pressures, are selected as the key areas. One reason for the selection of six key areas is that the air leakages happen adjacent to these six key areas. Roberge et al.[37] used thermal imaging for leak detection of FFR and found that regions near the nasal bridge, cheekbone, and chin, having bony prominences and thin overlying skin, accounted for most leak sites. It may imply that an even distribution of the pressure on the contact area causes the air leakages. Another reason is that high pressures on the six key areas make subjects feel discomfort.[1] Thus, a feasible way of validation is to compare the pressure values for the same key area from experiment and simulation.

Note that in this study all headforms are modeled as multilayer deformable models. This deformability is critical for the simulation approach to ensure high fidelity. However, in the experiment part, the headform prototypes are nondeformable. This is not contradictory for validation because the cost of deformable headform prototypes is too expensive. The simulation results are strongly correlated with the experiment

TABLE III. Contact Pressure Differences and SD (M Pa) for the Two Respirators of the Two-Size System

	Key Area					
Headform	**1 (SD)**	**2 (SD)**	**3 (SD)**	**4 (SD)**	**5 (SD)**	**6 (SD)**
			Two-Size – Medium			
Large	0.0002 (0.0050)	–0.0004 (0.0036)	–0.0088 (0.0057)	0.0003 (0.0018)	–0.0019 (0.0003)	–0.0025 (0.0034)
Medium	–0.0037 (0.0055)	0.0087 (0.0003)	0.0019 (0.0030)	0.0005 (0.0008)	0.0016 (0.0015)	0.0020 (0.0023)
Small	–0.0028 (0.0028)	0.0033 (0.0031)	0.0041 (0.0053)	0.0021 (0.0005)	–0.0029 (0.0015)	–0.0036 (0.0071)
Short/wide	–0.0021 (0.0026)	–0.0007 (0.0007)	–0.0087 (0.0013)	–0.0031 (0.0014)	0.0023 (0.0006)	0.0019 (0.0010)
Long/narrow	–0.0007 (0.0024)	–0.0011 (0.0006)	–0.0013 (0.0055)	0.0009 (0.0014)	–0.0018 (0.0031)	–0.0006 (0.0007)
			Two-Size – Small			
Large	0.0030 (0.0010)	0.0004 (0.0041)	–0.0026 (0.0034)	0.0021 (0.0015)	–0.0011 (0.0012)	–0.0042 (0.0026)
Medium	–0.0051 (0.0086)	0.0008 (0.0016)	–0.0008 (0.0026)	–0.0017 (0.0036)	–0.0060 (0.0023)	–0.0064 (0.0041)
Small	0.0003 (0.0009)	–0.0074 (0.0022)	–0.0096 (0.0052)	–0.0075 (0.0068)	–0.0025 (0.0035)	–0.0032 (0.0023)
Short/wide	0.0052 (0.0020)	0.0072 (0.0025)	–0.0061 (0.0013)	–0.0004 (0.0017)	–0.0086 (0.0010)	–0.0017 (0.0008)
Long/narrow	–0.0021 (0.0034)	0.0041 (0.0014)	–0.0076 (0.0009)	–0.0079 (0.0014)	–0.0054 (0.0026)	–0.0059 (0.0008)

TABLE IV. Contact Pressure Differences and SD (M Pa) for Three Respirators of the Three-Size System

	Key Area					
Headform	**1 (SD)**	**2 (SD)**	**3 (SD)**	**4 (SD)**	**5 (SD)**	**6 (SD)**
			Three-Size – X - Large			
Large	0.0040 (0.0010)	0.0038 (0.0023)	0.0007 (0.0012)	0.0009 (0.0018)	0.0052 (0.0007)	0.0079 (0.0039)
Medium	0.0055 (0.0021)	0.0005 (0.0010)	–0.0015 (0.0019)	0.0007 (0.0035)	–0.0018 (0.0029)	–0.0007 (0.0010)
Small	0.0005 (0.0006)	–0.0010 (0.0024)	0.0005 (0.0027)	0.0054 (0.0050)	–0.0007 (0.0017)	–0.0019 (0.0020)
Short/wide	–0.0020 (0.0014)	–0.0008 (0.0019)	–0.0013 (0.0038)	0.0009 (0.0016)	0.0017 (0.0009)	–0.0064 (0.0008)
Long/narrow	0.0006 (0.0004)	0.0034 (0.0013)	0.0093 (0.0014)	0.0028 (0.0012)	0.0044 (0.0011)	–0.0055 (0.0028)
			Three-Size – Large/Medium			
Large	0.0018 (0.0007)	–0.0013 (0.0009)	0.0034 (0.0019)	–0.0013 (0.0005)	0.0009 (0.0016)	–0.0051 (0.0001)
Medium	0.0051 (0.0020)	0.0024 (0.0004)	–0.0015 (0.0047)	–0.0028 (0.0027)	–0.0017 (0.0027)	0.0006 (0.0014)
Small	0.0016 (0.0024)	0.0019 (0.0004)	–0.0010 (0.0004)	0.0023 (0.0036)	0.0027 (0.0021)	–0.0003 (0.0011)
Short/wide	–0.0012 (0.0041)	–0.0036 (0.0029)	0.0026 (0.0017)	–0.0021 (0.0028)	–0.0004 (0.0020)	–0.0038 (0.0036)
Long/narrow	–0.0007 (0.0021)	0.0006 (0.0003)	0.0046 (0.0022)	–0.0026 (0.0018)	0.0017 (0.0004)	–0.0021 (0.0017)
			Three-Size – Small			
Large	0.0051 (0.0035)	–0.0001 (0.0017)	–0.0010 (0.0008)	0.0012 (0.0030)	0.0017 (0.0034)	0.0007 (0.0008)
Medium	–0.0011 (0.0012)	–0.0011 (0.0019)	0.0004 (0.0023)	0.0018 (0.0012)	–0.0009 (0.0018)	0.0002 (0.0019)
Small	–0.0002 (0.0015)	–0.0021 (0.0021)	–0.0003 (0.0012)	0.0007 (0.0006)	0.0001 (0.0014)	–0.0051 (0.0027)
Short/wide	0.0046 (0.0013)	0.0008 (0.0034)	–0.0053 (0.0072)	0.0062 (0.0007)	–0.0016 (0.0025)	–0.0019 (0.0018)
Long/narrow	0.0010 (0.0014)	0.0000 (0.0001)	0.0035 (0.0018)	0.0043 (0.0033)	0.0020 (0.0014)	0.0016 (0.0014)

results. We believe that the coefficient of correlation will be larger if one uses deformable headform prototypes.

Several sources may contribute to the error between computational and experimental results. In this study, FE models of headforms are deformable with multiple layers, while experimental results are from headform prototypes with a non-deformable surface due to the high cost of deformable headforms. Another source is from numerical errors from the LS-DYNA solver for large displacement simulation. The large displacements of both the FFR and headforms commonly cause the numerical algorithm to be unstable. Another error source is from the experiment, as contact pressure values are very sensitive to the locations of sensors. The shape of the contact area is like a doughnut, and the width of the cross section of the doughnut is less than 10 mm. Therefore, the pressure gradient is more than 0.003 MPa/mm in the cross direction of the contact area. The high pressure gradient contributes to the difficulty of ensuring the same location for experiment and simulation. In addition, accurate material properties are critical for simulation models. All material properties in this study are from the literature, and this may also contribute some error.

Contact pressure is one important factor that affects both respirator comfort and fit. This work is the first step to understand the interaction between respirators and headforms. The ultimate goal of this research is to develop predictive models for assessing respirator comfort and fit by eliminating physical prototypes and experiments. Future work includes (1) validating simulation models using human subjects, (2) investigating contact pressure sensitivity to various factors, (3) adding human head movement and facial deformation in the model, and (4) developing a final fit model and comfort model.

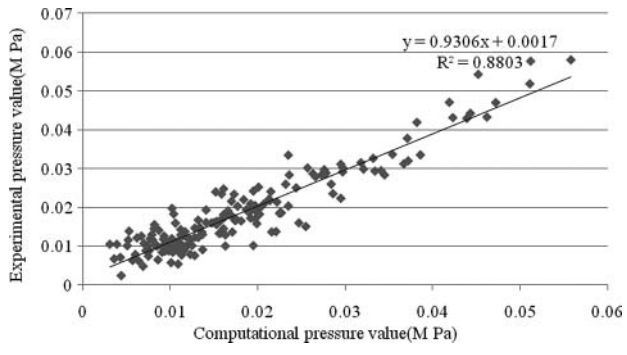

FIGURE 13. Correlation of experiment and simulation results.

CONCLUSIONS

We present a computational approach to simulate the contact pressure between an FFR and a headform and an experimental approach to validate the simulation models. High-fidelity headform FE models and deformable FE respirator models from rough 3D scanned data were developed. It was shown that simulation results match experiment results very well. There is a strong correlation between computational and experimental results ($R^2 = 0.88$). By comparing the pressure values from simulations and experiments, we have validated the simulation models. It was shown that high-fidelity models play an important role in simulation.

ACKNOWLEDGMENTS

This research was partly supported by the National Institute for Occupational Safety and Health (NIOSH) project (Contract No. 254-2009-M-31878).

REFERENCES

1. **Snook, S.H., W.C. Hinds, and W.M.A. Burgess:** Respirator comfort: Subjective response to force applied to the face. *Am. Ind. Hyg. Assoc. J. 27*:93–97 (1966).
2. **Manninen, A., T. Klen, and P. Pasanen:** Evaluation of comfort and seal leakages of several respirators used in agricultural work. *Am. Ind. Hyg. Assoc. J. 27*(*49*):280–285 (1988).
3. **Shimozaki, S., P. Harber, T. Barrett, and P. Loisides:** Subjective tolerance of respirator loads and its relationship to physiological effects. *Am. Ind. Hyg. Assoc. J. 49*:108–116 (1988).
4. **Damascene, J., A. Abeysekera, and S. Houshang:** Ergonomics aspects of personal protective equipment: Its use in industrially developing countries. *J. Hum. Ergon. 17*:67–79 (1988).
5. **White, M.K.:** Work tolerance and subjective responses to wearing protective clothing and respirators during physical work. *Ergonomics 32*(*9*):1111–1123 (1989).
6. **Jelier, P., and S. Hughes**: Mechanical and Anthropometric Characteristics of Soft Tissue Layers in the Head and Maxillofacial Region, Using Combined Mechanical and Ultrasound Techniques. [Unpublished paper] Guildford, U.K.: University of Surrey, 1994.
7. **U.S. Army Research Laboratory**: Biomechanical Comfort Modeling of the M40 Military Gas Mask by C. Lu. [Unpublished] Aberdeen Proving Ground, Md.: Army Research Laboratory, 1995.
8. **Akbar-Khanzadeh, F., M.S. Bisesi, and R.D. Rivas:** Comfort of personal protective equipment. *Appl. Ergonom. 26*(*3*):195–198 (1995).
9. **U.S. Army Research Laboratory, Human Engineering and Research Directorate**: *Relationship of Protective Mask Seal Pressure to Fit Factor and Head Harness Strap Stretch* by K.S. Cohen. Technical Report ARL-TR-2070. Aberdeen Proving Ground, Md.: Army Research Laboratory, 1999.
10. **Mols, G., B.C. Von Ungern-Sternberg, E.C. Rohr, C. Haberthur, K. Geiger, and J. Guttmann:** Respiratory comfort and breathing pattern during volume proportional assist ventilation and pressure support ventilation: A study on volunteers with artificially reduced compliance. *Crit. Care Med. 28*(*6*):1940–1946 (2000).
11. **U.S. Army Research Laboratory, Human Engineering and Research Directorate**: Modeling the Interface between a Respirator and the Human Face, by D. Piccione, E.T. Moyer Jr., and K.S. Cohen. Final Report. Aberdeen Proving Ground, Md.: Army Research Laboratory, 1997.
12. **Zhuang, Z., and B. Bradtmiller:** Head and face anthropometric survey of U.S. respirator users. *J. Occup. Environ. Hyg. 2*:567–576 (2005).
13. **Zhuang, Z., C. Coffey, and A.R. Berry:** The effect of subject characteristics and respirator features on respirator fit. *J. Occup. Environ. Hyg. 2*:641–649 (2005).
14. **Zhuang, Z., B. Bradtmiller, and R.E. Shaffer:** New respirator fit test panels representing the current U.S. civilian work force. *J. Occup. Environ. Hyg. 4*:647–659 (2007).
15. **Bitterman, B.H.**: Application of Finite Element Modeling and Analysis to the Design of Positive Pressure Oxygen Masks. Master's thesis, Air Force Institute of Technology, Wright-Patterson Air Force Base, Ohio, 1991.
16. **Zhuang, Z., and D. Viscusi**: A New Approach to Developing Digital 3-D Headforms. Paper presented at the SAE Digital Human Modeling for Design and Engineering Symposium, June 14–17, 2008, Pittsburgh, Pa.
17. **Yang, J., J. Dai, and S. Zhang:** Simulating the interaction between a respirator and a headform using LS-DYNA. *Comput. Aided Des. Appl. 6*(*4*):539–551 (2009).
18. **Dai, J., J. Yang, and S. Zhuang:** Sensitivity analysis of important parameters affecting contact pressure between a respirator and a headform. *Int. J. Ind. Ergonom. 41*(*3*):268–279 (2011).
19. **Zhuang, Z., S. Benson, and D. Viscusi:** Digital 3-D headforms with facial features representative of the current US workforce. *Ergonomics 53*(*5*):661–671 (2010).
20. **Lei, Z., J. Yang, and S. Zhuang:** Contact pressure of N95 filtering facepiece respirators using finite element method. *Comput. Aided Des. Appl. 7*(*6*):847–861 (2010).
21. **Waters, K.:** Physical model of facial tissue and muscle articulation derived from computer tomography data. In *Visualization in Biomedical Computing*, Vol. 1808. Bellingham, Wash.: SPIE, 1992. pp. 574–583.
22. **Keeve, E., S. Girod, R. Kikinis, and B. Girod:** Deformable modeling of facial tissue for craniofacial surgery simulation. *Comput. Aided Surg. 3*(*5*):228–238 (1998).
23. **Hart, R.T., V.V. Hennebel, N. Thongpreda, W. Buskirk, and R.C. Anderson:** Modeling the biomechanics of the mandible: A three-dimensional finite element study. *J. Biomech. 25*(*3*):261–286 (1992).
24. **Couteau, B., Y. Payan, and S. Lavallee**: (2000) The mesh-matching algorithm: An automatic 3D mesh generator for finite element structures. *J. Biomech. 33*(*8*):1005–1009 (2000).
25. **Payan, Y., M. Chabanas, X. Pelorson, et al.:** Biomechanical models to simulate consequences of maxillofacial surgery. *C. R. Biol. 325*(*4*):407–417 (2002).
26. **Luboz, V., M. Chabanas, P. Swider, and Y. Payan:** Orbital and maxillofacial computer aided surgery: Patient-specific finite element models to predict surgical outcomes. *Comput. Methods Biomech. Biomed. Engin. 8*(*4*):259–265 (2005).
27. **Zhang, Y., T. Sin, and E. Sung:** "Anatomy-Based Human Face Reconstruction Using Multi-layer Deformation." Presentation at the 13th International Conference in Central Europe on Computer Graphics, Visualization and Computer Vision 200, Plzen, Czech Republic, Jan. 1– Feb. 4, 2005.
28. **Barbarino, G., M. Jabareen, J. Trzewik, and E. Mazza**: Physically based finite element model of the face. In *Biomedical Simulation*, Proceedings of the 4th International Symposium, London, July 7–8, 2008. Berlin/Heidelberg: Springer, 2008.
29. **Hung, A., K. Mithraratne, M. Sagar, and P. Hunter:** Multilayer soft tissue continuum model: Towards realistic simulation of facial expressions. *Proceedings World Academy of Science Engineering and Technology 54*:134–138 (2009).
30. **Takema, Y., Y. Yorimoto, M. Kawai, and G. Imokava:** Age-related changes in the elastic properties and thickness of human facial skin. *Br. J. Dermatol. 131*:641–648 (1994).
31. **De Greef, S., P. Claes, D. Vandermeulen, W. Mollemans, P. Suetens, and G. Willems:** Large-scale in-vivo Caucasian facial soft tissue thickness database for craniofacial reconstruction. *Forensic Sci. Int. 159*(*Suppl 1*):S126–S146 (2006).
32. **Schaff, A.J., and A.A. Ogale:** Tensile viscoelasitic properties of spunbonded nonwoven polypropylene backing. *Textile Res. J. 61*:386–392. (1991).
33. **Gladilin, E.:** "Biomechanical Modeling of Soft Tissue and Facial Expressions for Craniofacial Surgery Planning." Ph.D. diss., Department of Mathematics and Computer Science, Free University Berlin, Berlin, Germany, 2002.
34. **Fung, Y.C.:** *Biomechanics—Mechanical Properties of Living Tissues*, 2nd ed. New York: Springer-Verlag, 1993.
35. **Duck, F.:** *Physical Properties of Tissues: A Comprehensive Reference Book*. London: Academic Press, 1991.
36. **Hallquist, J.:** *LS-DYNA Theoretical Manual*. Livermore, Calif.: Livermore Software Corporation, 2006.
37. **Roberge, R J., W.D. Monaghan, A.J. Palmiero, R. Shaffer, and M. Bergman:** Infrared imaging for leak detection of N95 filtering facepiece respirators: A pilot study. *Am. J. Ind. Med. 54*(*8*):628–636 (2011).